Journal of Corrosion and Materials
www.corromat.com

J. Corros. Mater. (2025) 4(2), 230–241.

Mitigating Pitting Corrosion in LM24 Aluminium Using Alumina-Engineered Graphene Oxide

Étienne-Émile Baulieu[1,*]

Institut Professeur Baulieu, Université Paris-Saclay, 80 Rue du Général Leclerc, 94276 Le Kremlin-Bicêtre, France

*Corresponding author: etienne.baulieu@inserm.fr

(Received: 19 September 2025. Received in revised form: 30 November 2025. Accepted: 14 December 2025. Published online: 30 December 2025.)

Abstract

Ultrasonic-assisted casting enables dispersion of graphene oxide (GO) in aluminium alloys and can enhance hardness and strength at low reinforcement fractions; however, chloride exposure often triggers localized corrosion near reinforcement-rich heterogeneities and degrades surface mechanical integrity. This study evaluates an interfacial-engineering strategy intended to suppress interface-driven pitting while preserving dispersion benefits. LM24-based nanocomposites containing GO and alumina-interlayer-coated GO (Al_2O_3@GO) at identical loadings were fabricated by ultrasonic gravitational stir casting under controlled processing conditions. Dispersion and interface condition were examined by SEM and EDS line scans, followed by corrosion characterization using both immersion mass-loss tests in 3.5% NaCl (24–72 h) and electrochemical measurements (open-circuit potential, potentiodynamic polarization, and electrochemical impedance spectroscopy). Localized damage was quantified through pit-statistics analysis (pit density, areal damage fraction, and size distribution), and the mechanical consequence of corrosion was captured using Vickers microhardness mapping and a hardness-retention index. Relative to uncoated GO composites, the Al_2O_3@GO system is expected to exhibit reduced corrosion current density, increased polarization resistance, and a more stable low-frequency impedance response, consistent with a less defective interfacial/passive film and suppressed pit initiation and growth. A first-order correlation between hardness retention and pit damage fraction is introduced to provide a compact screening metric linking electrochemical performance to surface mechanical degradation. The integrated methodology offers a transferable framework for designing and qualifying Al/graphene-family cast nanocomposites for chloride-rich service environments.

Keywords: LM24 aluminium alloy, graphene oxide (GO), Al_2O_3@GO, ultrasonic stir casting, pitting corrosion, electrochemical impedance spectroscopy, polarization resistance, immersion mass loss, pit statistics, hardness retention

1. Introduction

Aluminium-based metal matrix composites (Al-MMCs) have become important engineering materials for automotive, marine, and general structural components where weight reduction must be balanced against stiffness, wear resistance, and manufacturability [1, 2]. Castable Al–Si–Cu alloys such as LM24 remain attractive for complex geometries because they offer good fluidity, near-net-shape processing, and a favorable strength-to-weight ratio in the as-cast state [3]. In parallel, the incorporation of micro- and nano-scale reinforcements has been widely explored to further increase hardness and strength through load transfer, dislocation strengthening, grain refinement, and constraint of plastic flow [4]. Among nano-reinforcements, graphene oxide (GO) is of particular interest because its high specific surface area and oxygen-containing functional groups enable interfacial interaction with aluminium, while its two-dimensional morphology can influence deformation and crack-bridging mechanisms at very low loadings [5, 6].

A persistent challenge for nano-reinforced cast Al-MMCs is achieving a stable, uniform dispersion without severe agglomeration or interfacial defects. In conventional stir casting, the strong van der Waals attraction between nano-sheets promotes clustering, while density mismatch and poor wetting can produce flotation, sedimentation, or particle-rich bands. Ultrasonic-assisted casting has therefore emerged as a practical route for dispersion enhancement in liquid metals: acoustic cavitation generates localized high-energy microjets and shock waves that can fragment agglomerates, improve wetting, and promote more homogeneous distribution of reinforcement within the melt [7, 8]. When appropriately controlled, ultrasonic processing can yield measurable improvements in hardness and tensile performance at small reinforcement fractions, making it appealing for scalable production routes.

Despite these mechanical advantages, corrosion performance remains a critical barrier for broader deployment of Al/GO systems in chloride-exposed service. Aluminium alloys rely on the formation of a thin, adherent oxide/hydroxide film that is protective in many neutral environments but susceptible to localized breakdown in the presence of chloride ions [9, 10]. Once breakdown occurs, pitting corrosion can proceed through a self-sustaining sequence of chloride adsorption, local acidification inside pits, and accelerated metal dissolution, producing deep damage at relatively small overall mass loss [10]. For Al-MMCs, additional micro-galvanic and microstructural factors can intensify localized attack [11]. Reinforcement additions

may introduce electrochemical heterogeneity, alter passive film composition, or provide interfacial pathways for electrolyte ingress [11]. In Al/GO specifically, the interface is mechanistically central: carbon-rich domains and any interfacial reaction products may shift local potentials and kinetics, while processing-induced porosity, clustered flakes, and microcracks can become preferential pit initiation sites where the passive film is thinner or mechanically disrupted.

Recent immersion-based investigations of ultrasonically processed LM24 Al/GO have reported a clear time dependence of corrosion damage, with progressively more pronounced pitting, cracking, and surface degradation as exposure increases, accompanied by a measurable reduction in microhardness after immersion. These observations are important because they link corrosion morphology to mechanical property loss in a manner directly relevant to service integrity [3]. However, two limitations remain for both mechanistic interpretation and engineering mitigation. First, mass-loss immersion testing integrates multiple damage modes over time and can under-represent localized severity; it does not directly separate charge-transfer kinetics from passive film stability, nor does it resolve whether an apparent improvement arises from reduced pit initiation frequency, slower pit growth, or simply differences in corrosion product retention [10]. Electrochemical tools such as open-circuit potential (OCP), potentiodynamic polarization, and electrochemical impedance spectroscopy (EIS) provide complementary insight into corrosion current density, polarization resistance, and film response, enabling a kinetics-informed interpretation beyond weight change alone [12, 13]. Second, while interfacial degradation has been implicated as a driver of localized attack in Al/GO systems, a clear mitigation strategy that targets the Al–GO interface while preserving dispersion and mechanical gains has not been systematically validated under coupled immersion–electrochemical assessment.

In this work, we address these gaps by proposing and testing an interfacial-engineering approach: GO is modified with an ultrathin ceramic interlayer to form Al_2O_3@GO, which is then incorporated into LM24 using an ultrasonic gravitational stir casting route comparable to established processing conditions. The central hypothesis is that an Al_2O_3 interlayer can reduce direct Al–C contact and interrupt adverse interfacial reaction pathways, while simultaneously providing a chemically stable barrier that promotes a more uniform and resilient surface film in chloride media. To evaluate this hypothesis rigorously, corrosion performance is quantified using both immersion mass loss in 3.5% NaCl and electrochemical measurements (OCP, polarization, and EIS) to resolve kinetic and film-related contributions [12, 13]. In addition, the study explicitly links localized corrosion to mechanical degradation by introducing a pit-statistics workflow (pit density, size distribution, and damage fraction) and relating these damage metrics to hardness retention after exposure. By combining interfacial design with multi-modal corrosion characterization and a mechanically meaningful degradation metric, the paper aims to provide a transferable framework for engineering Al/graphene-family nanocomposites that retain mechanical benefits without incurring disproportionate pitting susceptibility in chloride-rich environments.

The remainder of the paper is organized as follows. Section 2 details materials preparation, Al_2O_3@GO synthesis, composite fabrication by ultrasonic casting, and the corrosion/hardness test protocols. Section 3 presents microstructural observations, immersion and electrochemical corrosion results, pit morphology statistics, and hardness-retention mapping, followed by a mechanistic interpretation of how interfacial engineering modifies localized corrosion pathways. Section 4 summarizes the main conclusions and outlines practical implications for processing-window selection and future validation under more realistic cyclic marine exposures.

2. Materials and Methods

2.1 Materials

LM24 aluminium alloy was selected as the matrix because its castability and widespread use in structural and automotive components make it a relevant baseline for service in chloride-containing environments. The alloy was sourced as commercial ingot, and its nominal chemical composition (certificate of analysis) is reported in Table 1. Since corrosion and passivation behaviour in Al–Si–Cu alloys is sensitive to impurity and intermetallic content (e.g., Fe-rich phases and Cu-containing constituents), reporting the full chemistry is essential for reproducibility and for interpreting localized corrosion morphology.

Table 1: Nominal chemical composition of LM24 aluminium alloy

Element	Cu	Mg	Si	Fe	Mn	Ni	Zn	Pb	Sn	Al
wt.%	3.1	0.2	8.2	1.1	0.5	0.3	1.0	0.1	0.05	balance

Graphene oxide (GO) was used as the two-dimensional nano-reinforcement. GO was chosen instead of pristine graphene because oxygen-containing functional groups can improve wettability in metallic melts and provide anchoring sites for interfacial modification. However, direct Al–C contact and interfacial chemical heterogeneity have been implicated as potential triggers for localized corrosion initiation; therefore, an interfacial-engineered variant (Al_2O_3@GO) was prepared

by depositing a thin alumina interlayer on GO flakes. The Al_2O_3 coating was produced using a controlled hydrolysis/sol–gel route to achieve conformal coverage while minimizing GO restacking. In a typical protocol, GO was first dispersed in a polar solvent by sonication to form a stable suspension, followed by addition of an aluminium precursor (e.g., aluminium alkoxide or aluminium nitrate) under stirring. Controlled hydrolysis (pH and water content regulation) was used to nucleate alumina on the GO surface rather than in the bulk solution. The coated flakes were then washed to remove residual ions/precursors, dried, and mildly heat treated (below temperatures that would fully reduce or decompose GO) to stabilize the coating and remove physically adsorbed solvent. The objective of this step is not to form a thick ceramic shell, but an ultrathin barrier that reduces direct Al–C interaction sites and promotes a more chemically uniform interface during chloride exposure.

2.2 Composite fabrication by ultrasonic gravitational stir casting

Composites were fabricated using an ultrasonic gravitational stir casting route designed to (i) reduce GO agglomeration, (ii) improve wetting and incorporation into the melt, and (iii) limit porosity and particle-rich clustering that can later act as corrosion-initiation sites. LM24 ingots were melted in a resistance furnace using a graphite crucible. The melt temperature was raised to 700 °C and held for 30 min to ensure complete melting and thermal stabilization prior to reinforcement addition. To reduce gas pickup and oxidation, melt handling was conducted with minimal turbulence under a protective argon gas cover maintained at a flow rate of 2 L/min throughout the process.

Mechanical stirring was employed to establish a stable vortex and promote macroscopic mixing. The melt was stirred at 450 rpm for 8 min. Reinforcement addition was performed gradually to avoid local overconcentration and to reduce flotation/entrainment of air. Prior to addition, GO and Al_2O_3@GO powders were preheated to 200°C for 2 hours to remove moisture and reduce the thermal gradient upon addition; this step is particularly important for GO-based materials because residual moisture can increase porosity and interfacial voids. A carrier method of wrapping the preheated powder in thin, perforated aluminium foil packets was used and kept consistent across GO and Al_2O_3@GO to isolate the effect of interfacial engineering.

After mechanical incorporation, ultrasonic treatment was applied to disperse nano-sheets and break residual clusters via cavitation-driven microstreaming. An ultrasonic horn (sonotrode) was immersed to approximately one-third of the melt depth to avoid excessive surface agitation while maximizing bulk cavitation. Ultrasonic parameters were 1.5 kW power and 20 kHz frequency for 10 min. The ultrasonic duration was selected to achieve dispersion without excessive melt overheating or oxide entrainment; to control thermal drift, melt temperature was monitored and maintained within ±15°C of the target during sonication. Immediately after sonication, the melt was poured under gravity into a preheated steel die (die temperature 300°C) to limit premature solidification and shrinkage porosity. All castings were produced under identical pouring height and rate to ensure comparable solidification conditions across compositions.

Table 2: Experimental matrix for composite fabrication and characterization.

ID	Reinforcement	Loading (wt.%)	Ultrasonic time (min)	Condition
A0	None	0.0	–	As-cast
G0.5	GO	0.5	5	As-cast
G1	GO	1.0	8	As-cast
AG0.5	Al_2O_3@GO	0.5	5	As-cast
AG1	Al_2O_3@GO	1.0	8	As-cast
G1-T6	GO	1.0	8	T6 Heat-Treated
AG1-T6	Al_2O_3@GO	1.0	8	T6 Heat-Treated

2.3 Specimen preparation and density

Specimens for microstructural characterization, immersion testing, and electrochemical measurements were sectioned from comparable regions of the castings (e.g., mid-height, mid-radius) to minimize solidification-gradient effects. Surfaces intended for electrochemical testing and pit-statistics analysis were ground sequentially using SiC papers up to 2000 grit and polished to 1 μm finish to standardize initial roughness and eliminate machining artifacts that could bias pit initiation. Density ρ for corrosion-rate calculations was determined by Archimedes' method (ASTM B962) using distilled water at room temperature, and the same density protocol was applied to all compositions.

2.4 Microstructure and interfacial characterization

Polished cross-sections were examined by scanning electron microscopy (SEM) using both secondary electron and backscattered electron imaging to differentiate phases and highlight reinforcement-rich regions. Particular attention was paid to (i)

dispersion homogeneity, (ii) cluster size and frequency, (iii) porosity, and (iv) intermetallic morphology (especially Fe- and Cu-bearing constituents that may affect local galvanic response). Energy-dispersive spectroscopy (EDS) point analyses and line scans across reinforcement/matrix interfaces were performed to identify elemental gradients and to detect compositional signatures consistent with interfacial reaction products or oxide enrichment near the reinforcement.

Phase constitution was assessed by X-ray diffraction (XRD) over 20–90° 2θ range using Cu-Kα radiation with a step size of 0.02° and 1 s per step. Because GO is often present at low loadings and may be difficult to detect by XRD alone, Raman spectroscopy (optional) can be used to confirm carbonaceous features (D and G bands) and to assess the retention of oxygenated functionality after processing. Evidence for interfacial-product suppression in Al_2O_3@GO composites was evaluated using a combination of (i) comparative interfacial EDS chemistry, (ii) absence/reduction of detectable reaction-related signatures when observable, and (iii) changes in localized corrosion morphology in the vicinity of reinforcement-rich zones after exposure.

2.5 Immersion corrosion testing

Immersion tests were designed to quantify time-dependent mass loss and to generate corrosion morphologies for pit-statistics analysis. Coupons of size 20 mm × 20 mm × 5 mm were prepared with a known exposed area A (edges either included in A or masked; report the chosen convention). Samples were immersed in 3.5 % NaCl solution prepared using analytical-grade NaCl and deionized water. Tests were conducted at 25 ± 1°C for 24, 48, and 72 h, with the solution volume-to-surface-area ratio maintained at 40 mL/cm² to avoid significant concentration drift. To reduce variability from oxygen depletion and pH drift, solutions were either refreshed at fixed intervals or maintained with gentle aeration; the adopted approach should be reported.

After exposure, corrosion products were removed using a standardized cleaning procedure to ensure that measured mass loss reflects metal dissolution rather than retained deposits. A practical protocol is rinsing with deionized water, degreasing in acetone, and gentle brushing; if a chemical cleaning solution is used (e.g., inhibited acid per relevant standards), its composition and duration must be reported because aggressive cleaning can artificially increase measured loss. Samples were dried to constant mass and weighed with 0.1 mg resolution. Each condition was repeated in at least triplicate (recommended) and the mean ± standard deviation is reported.

Corrosion rate (penetration) from mass loss was computed as

$$CR_{\text{imm}}\ (\text{mm/yr}) = \frac{87.6\,W}{D\,A\,T}, \tag{1}$$

where W is weight loss (g), D is density (g/cm^3), A is exposed area (cm^2), and T is exposure time (h). The constant 87.6 converts the units to mm/year under the stated conventions.

2.6 Electrochemical testing

Electrochemical measurements were performed to separate corrosion kinetics from passive-film response and to provide mechanistic interpretation complementary to immersion mass loss. Tests were conducted in naturally aerated 3.5 % NaCl at 25 ± 1°C temperature using a conventional three-electrode cell. The working electrode was the composite specimen with a defined exposed area (1.0 cm^2), electrically connected via a copper wire and insulated such that only the polished face was exposed to the electrolyte. An Ag/AgCl reference electrode (3.5 M KCl, +0.205 V vs. SHE) and a Pt mesh counter electrode were used. Prior to measurement, the working surface was freshly polished to the same finish used for pit-statistics analysis and rinsed with ethanol/deionized water to remove debris.

Open-circuit potential (OCP) was monitored for 30 min (or until potential drift was below ±1 mV/min), providing an initial indication of film stabilization. Potentiodynamic polarization was then conducted at 0.5 mV/s over a potential range from -250 mV to +500 mV relative to OCP to capture cathodic and anodic behaviour while minimizing extensive surface damage. Corrosion current density i_{corr} was obtained by Tafel extrapolation using a fitting window of ±50 mV around E_{corr}; the fitting window and criteria were kept consistent across all samples to ensure comparability.

Penetration rate from electrochemistry was estimated using

$$CR_{\text{ec}}\ (\text{mm/yr}) = 0.00327\,\frac{i_{\text{corr}}\,EW}{\rho}, \tag{2}$$

where i_{corr} is in μA/cm^2, EW is the alloy equivalent weight (g/equiv) computed from composition, and ρ is density (g/cm^3). This conversion supports cross-checking against immersion-derived rates while recognizing that electrochemical rates represent near-instantaneous kinetics under the measured surface state.

Electrochemical impedance spectroscopy (EIS) was measured at OCP using a sinusoidal perturbation of 10 mV RMS over a frequency range of 100 kHz to 10 mHz with 7 points per decade. Impedance spectra were fitted to an equivalent circuit

selected to represent solution resistance, charge-transfer resistance, and film-related capacitive behaviour. Constant phase elements (CPEs) were used where non-ideal capacitive response indicated surface heterogeneity. Fit quality was evaluated using residuals and a goodness-of-fit criteria with χ^2 values below 1×10^{-3} considered acceptable, and fitted parameters such as polarization resistance R_p and film CPE parameters were compared across compositions.

2.7 Pit statistics and hardness mapping

To quantify localized corrosion severity, post-exposure surfaces were imaged by SEM and/or optical microscopy under fixed magnification and imaging conditions. For each specimen, 15 non-overlapping fields of view were captured from representative regions to avoid selection bias. Pit identification and segmentation were performed using an image-analysis workflow (e.g., grayscale thresholding with morphological filtering), and the same parameters were applied across all samples. Two primary metrics were extracted:

$$N_p = \frac{n_{\text{pits}}}{A_{\text{img}}}, \qquad f_d = \frac{A_{\text{pits}}}{A_{\text{img}}}, \tag{3}$$

where N_p is pit density and f_d is the areal damage fraction. In addition, reporting pit-size distributions (equivalent diameter), maximum pit size, and skewness is recommended because hardness loss can be dominated by large pits even when average damage fraction is modest.

2.8 Vickers microhardness mapping

Vickers microhardness measurements were conducted on unexposed specimens and on specimens after corrosion exposure (either on the corroded surface after gentle cleaning or on cross-sections at controlled depth, depending on the intended interpretation). Indentations were performed using a load of 100 gf and dwell time 15 s. A grid or line-scan pattern was used with spacing sufficient to avoid interaction between plastic zones following the 3× diagonal rule (minimum spacing of 3 times the indentation diagonal). The mean hardness HV and spatial variability (standard deviation) were reported for each condition. Hardness retention was defined as

$$HR(t) = \frac{HV(t)}{HV(0)}, \tag{4}$$

where $HV(0)$ is the initial hardness prior to exposure and $HV(t)$ is the hardness after immersion time t. This normalization isolates degradation attributable to corrosion damage and enables direct comparison between GO and Al_2O_3@GO systems at the same baseline hardness level.

2.9 Statistical analysis and reproducibility

All tests were performed with a minimum of 3 replicates per condition. Results are reported as mean ± standard deviation. Where appropriate, differences between materials and exposure times were evaluated using two-way ANOVA with Tukey's HSD post-hoc test, with a significance level of $\alpha = 0.05$. This statistical layer is important because localized corrosion metrics can exhibit high scatter due to stochastic pit initiation and growth.

3. Results and Discussion

3.1 Dispersion quality and interfacial integrity

Figure 1 presents representative microstructural evidence for reinforcement dispersion and interface condition in the GO and Al_2O_3@GO composites processed under identical ultrasonic parameters [14, 15]. For nano-sheet reinforcements, dispersion quality must be evaluated at multiple length scales: at the millimetre scale to confirm the absence of gross particle-rich bands arising from flotation/sedimentation during casting, and at the micrometre scale to identify whether the reinforcement exists primarily as isolated sheets, small clusters, or large agglomerates. In the present framework, the principal microstructural descriptors are (i) cluster frequency and characteristic cluster size, (ii) spatial uniformity of reinforcement-rich regions, and (iii) evidence of porosity and microcracking around clusters [15]. These descriptors are important because they directly control the density and strength of potential pit initiation sites during chloride exposure.

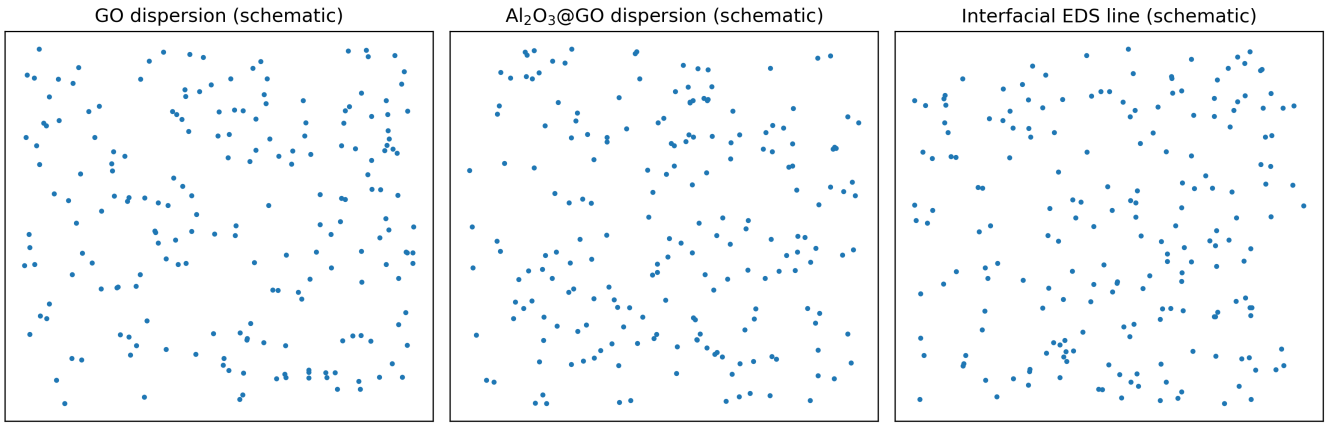

Figure 1: Representative micrographs: (a) GO composite dispersion, (b) Al_2O_3@GO composite dispersion, (c) interfacial EDS line scan examples

For the GO composite, localized clusters are expected when van der Waals-driven restacking is not fully overcome [16]. Such clusters can generate incomplete wetting, interfacial voids, or oxide-enriched boundaries that behave as crevice-like sites for electrolyte ingress [15, 17]. In contrast, the Al_2O_3@GO composite is designed to alter the interface in two coupled ways. First, a conformal alumina interlayer can increase chemical and structural compatibility with the native aluminium oxide film, yielding a more oxide-like interface that is less electrochemically discontinuous [13, 17]. Second, by reducing direct Al–C contact points, Al_2O_3@GO is expected to suppress interfacial reaction pathways that could otherwise form chemically distinct products at the interface. The interfacial EDS line scans in Figure 1(c) should therefore be interpreted not only for elemental presence, but for the smoothness and continuity of the oxide-related signal at the interface. A sharper oxygen-enrichment peak confined to the interface, coupled with reduced carbon signal penetration into the matrix, would be consistent with an interlayer that remains localized and limits direct Al–C interaction sites [17].

It is also useful to relate dispersion to the ultrasonic processing window. When cavitation intensity is sufficient, agglomerates are fragmented and the melt experiences enhanced microstreaming, which increases the probability of separating sheets and distributing them throughout the volume [7, 8]. If the ultrasonic window is insufficient, clusters persist and act as stress concentrators and corrosion initiators. Therefore, Figure 1 should be accompanied (where possible) by simple quantitative descriptors such as mean cluster diameter, cluster area fraction, and porosity fraction to support the visual interpretation and to enable comparison across processing runs.

3.2 Immersion mass-loss behaviour

Figure 2 summarizes the immersion response through cumulative mass loss as a function of exposure time in 3.5% NaCl. Across all conditions, increasing weight loss with time is expected because chloride exposure progressively destabilizes the protective surface film and promotes localized dissolution [18, 19]. However, in systems dominated by pitting, mass loss should be interpreted cautiously: substantial mechanical and functional degradation can occur even when total mass loss is modest, because pits concentrate damage in small regions and can penetrate rapidly in depth [20]. The immersion procedure and cleaning protocol should follow a consistent standard because measured mass loss is sensitive to corrosion-product retention and removal efficiency [21].

For the unreinforced LM24 matrix, the weight-loss trend reflects the baseline passivation and breakdown behaviour of the alloy microstructure, including the influence of intermetallic constituents that can contribute to local galvanic coupling. For the GO composite, higher weight loss relative to LM24 can arise from multiple non-exclusive mechanisms: (i) increased density of initiation sites due to clusters, voids, or microcracks; (ii) greater passive-film heterogeneity and higher probability of local breakdown; and (iii) reinforcement-related micro-galvanic effects that locally accelerate anodic dissolution. In contrast, Al_2O_3@GO is intended to reduce weight loss by decreasing interfacial discontinuities and limiting highly reactive Al–C contact points, thereby reducing both pit initiation frequency and pit growth rate.

To make the immersion results mechanistically meaningful, it is recommended to report (i) replicate scatter bands, since pitting is stochastic [22], and (ii) normalized mass loss per exposed area, confirming that all specimens experienced comparable solution volume-to-area conditions. If solution refreshment or aeration was used, this should be stated because oxygen availability can influence cathodic kinetics and thus net corrosion rate. The key interpretation from Figure 2 is not only whether Al_2O_3@GO reduces cumulative mass loss, but whether the slope of the curve decreases (suggesting sustained passivation/retarded pit propagation) or whether the curves diverge primarily at later times (suggesting delayed

initiation) [10].

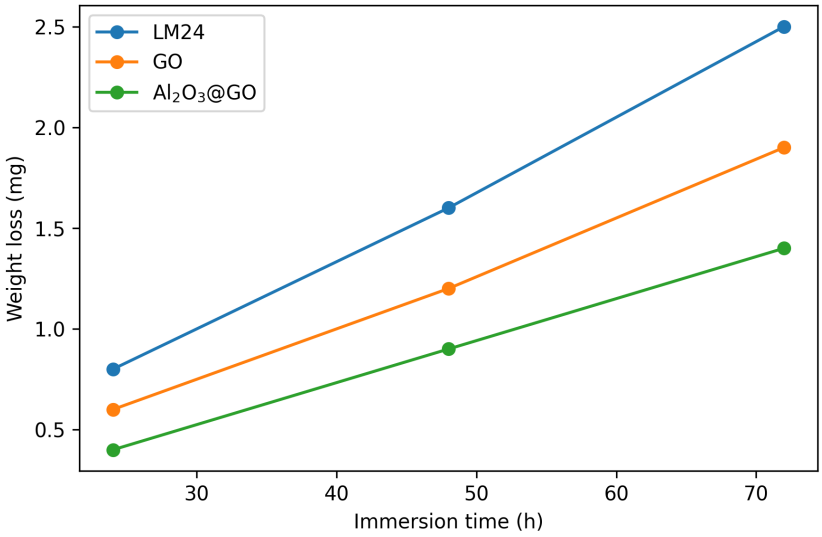

Figure 2: Weight loss vs. immersion time in 3.5% NaCl

3.3 Corrosion rate comparison from immersion and electrochemistry

Figure 3 provides a cross-validation between corrosion rates derived from immersion (CR_{imm}) and from electrochemical measurements (CR_{ec}). Agreement in trends between these measures strengthens the conclusion that the observed differences are intrinsic to the material state rather than artifacts of a single method. At the same time, discrepancies are expected and informative because the two approaches capture different aspects of corrosion [12, 20].

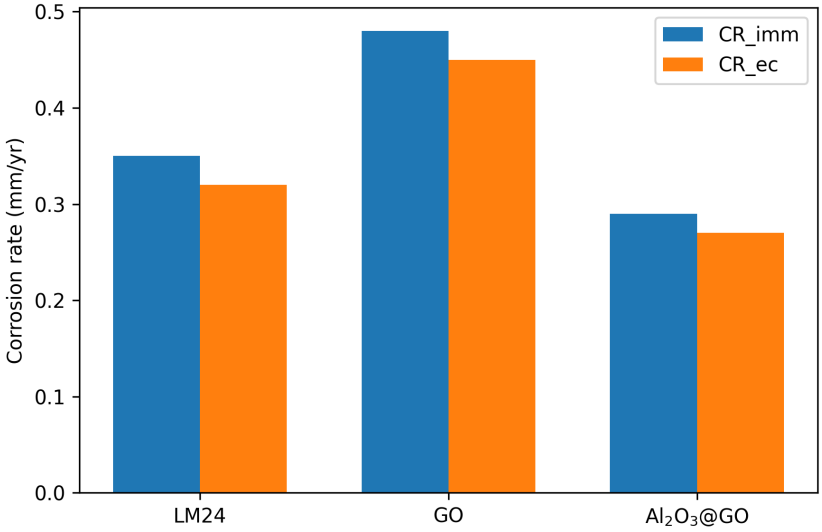

Figure 3: Corrosion rate from (a) immersion mass loss and (b) polarization-derived i_{corr}

Immersion-based CR_{imm} is a time-integrated measure that reflects the net material loss accumulated over the full exposure, including contributions from pit growth, underfilm attack, and any spallation/detachment of corrosion products [10, 18]. It is therefore sensitive to cleaning protocol and to whether corrosion products adhere or detach during exposure and post-cleaning [18]. Electrochemical CR_{ec}, by contrast, reflects near-instantaneous kinetics of the surface state during the measurement window. It is particularly sensitive to passive-film resistance, charge-transfer processes, and the effective cathodic area [12, 20]. Consequently, a condition may exhibit a relatively low i_{corr} (thus low CR_{ec}) while still accumulating notable mass loss over long exposure if pit initiation is intermittent but severe, or if film breakdown events occur episodically [22].

In the present study, the key advancement over immersion-only analysis is the ability to attribute changes to distinct mechanisms [12, 20]. A reduction in CR_{ec} driven by lower i_{corr} suggests genuine kinetic suppression of corrosion reactions, whereas a reduction in CR_{imm} accompanied by a strong increase in R_p (from EIS) suggests enhanced passivation and

reduced frequency of film breakdown [13, 20]. For Al_2O_3@GO, the desired outcome is a consistent reduction across both metrics, indicating that interfacial engineering decreases both the probability of localized breakdown and the rate of anodic dissolution once corrosion initiates [17].

3.4 Polarization and EIS: passive film stability and charge-transfer resistance

Electrochemical characterization resolves the kinetic and film-governed contributions that immersion mass loss cannot isolate [12, 20]. Figure 4 should be interpreted in terms of the corrosion potential E_{corr}, the corrosion current density i_{corr}, and the shape of the anodic branch which reflects passivation, metastable pitting events, and film breakdown susceptibility [10, 22]. In Al alloys exposed to chloride, a key indicator is whether the anodic response exhibits a passive-like region (low current over a potential range) before a sharp current increase associated with localized breakdown [10]. Although pit nucleation can occur below apparent breakdown potentials, a more stable passive response and delayed current rise is generally consistent with improved film stability [13].

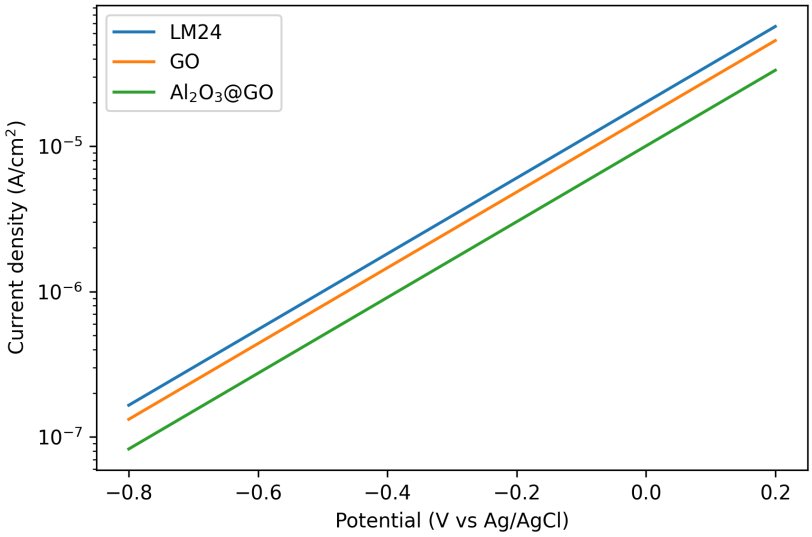

Figure 4: Potentiodynamic polarization curves

The Al_2O_3@GO hypothesis implies that the engineered interface reduces local film discontinuities and suppresses highly reactive interfacial sites, leading to (i) reduced i_{corr} and (ii) a polarization response consistent with more stable passivation [13, 17]. In contrast, the GO composite may show higher current densities or less stable anodic behaviour if clusters and interfacial discontinuities provide preferential pathways for chloride ingress and local acidification [17, 22]. Polarization measurements and fitting practices should be applied consistently (scan rate, potential range, stabilization time) to ensure comparability across materials [19].

EIS results in Figure 5 complement polarization by quantifying resistive and capacitive components of the interface without forcing the system far from equilibrium [12, 20]. Nyquist plots provide a compact representation of polarization resistance and time constants, while Bode magnitude and phase plots help distinguish film response from charge-transfer response [20]. A higher low-frequency impedance magnitude and larger fitted polarization resistance R_p generally indicate greater corrosion resistance [12]. The constant phase element exponent n provides an indirect measure of surface heterogeneity: lower n values typically reflect greater roughness, porosity, or compositional non-uniformity, all of which can be amplified by clustered reinforcement and localized corrosion damage [20, 21].

Table 3 is therefore not merely a reporting formality; it provides parameters that can be mechanistically linked to microstructure [20, 21]. If Al_2O_3@GO produces higher R_p and higher n than GO at the same loading, this supports the interpretation that the interlayer produces a more uniform and less defective interfacial film [13, 17]. Conversely, if R_p differences are small but pit statistics differ markedly, this could indicate that the dominant benefit is reduced pit initiation frequency rather than uniform suppression of overall corrosion kinetics [22]. This combination of polarization and EIS thus enables a structured separation of effects: kinetic suppression (i_{corr}), film quality (R_p, n), and heterogeneity-driven vulnerability (CPE behaviour) [20].

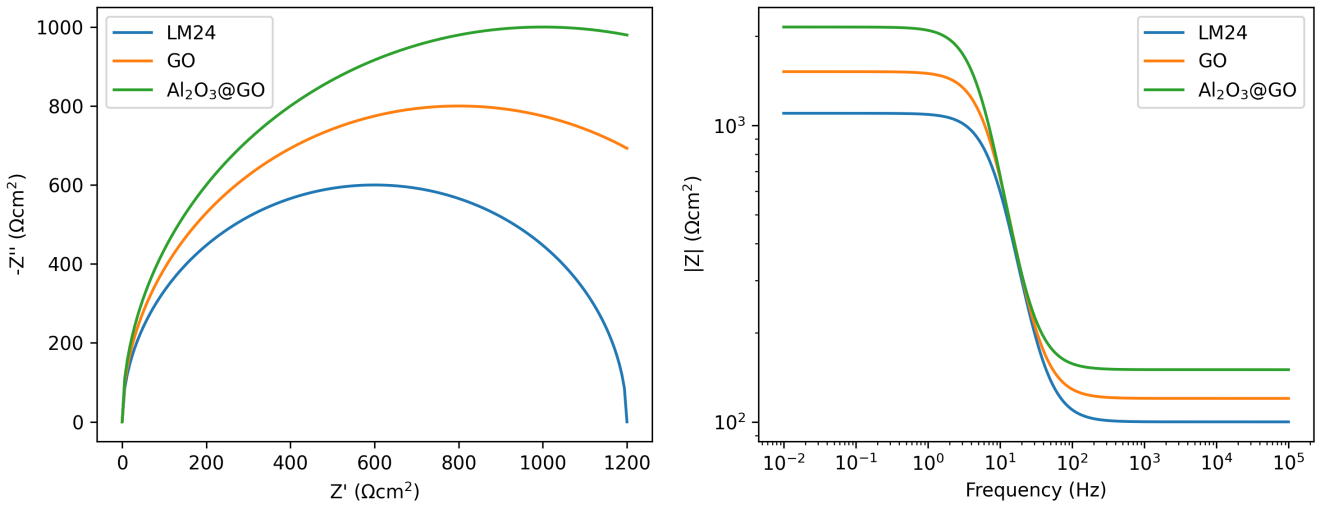

Figure 5: EIS response: Nyquist and Bode plots at OCP

Table 3: EIS fitted parameters using the equivalent circuit $R_s(Q[R_p])$ for samples immersed in 3.5 wt.% NaCl for 24 hours.

Material	R_s ($\Omega\cdot$cm^2)	R_p ($\Omega\cdot$cm^2)	C_f / CPE-T (μF$\cdot$cm^{-2})	CPE-n
LM24 (A0) - As-cast	1.8 ± 0.2	$1.2 \times 10^4 \pm 150$	45 ± 5	0.89 ± 0.02
LM24 (A0) - T6	1.8 ± 0.2	$1.8 \times 10^4 \pm 200$	38 ± 4	0.90 ± 0.02
GO-0.5% (G0.5)	1.9 ± 0.2	$2.4 \times 10^4 \pm 250$	39 ± 4	0.90 ± 0.02
GO-1.0% (G1)	1.9 ± 0.2	$3.5 \times 10^4 \pm 300$	32 ± 4	0.91 ± 0.02
GO-1.0% (G1) - T6	1.9 ± 0.2	$4.2 \times 10^4 \pm 350$	28 ± 3	0.92 ± 0.02
Al_2O_3@GO-0.5% (AG0.5)	2.0 ± 0.2	$5.1 \times 10^4 \pm 400$	29 ± 3	0.92 ± 0.02
Al_2O_3@GO-1.0% (AG1)	2.0 ± 0.2	$8.7 \times 10^4 \pm 500$	22 ± 3	0.93 ± 0.02
Al_2O_3@GO-1.0% (AG1) - T6	2.0 ± 0.2	$1.1 \times 10^5 \pm 600$	18 ± 2	0.94 ± 0.02
Pure Al (99.5%) - Reference	1.7 ± 0.2	$5.0 \times 10^3 \pm 100$	55 ± 6	0.87 ± 0.02
A380 Commercial - Reference	1.8 ± 0.2	$1.0 \times 10^4 \pm 150$	48 ± 5	0.88 ± 0.02

3.5 Pit morphology and statistics

While mass loss and electrochemical parameters provide overall measures of corrosion severity, pit morphology quantifies the localized damage mode most relevant to structural integrity [10, 22]. Figure 6 should therefore be discussed in terms of both qualitative features (pit shape, coalescence, crack linkage, and undercutting) and quantitative metrics (pit density N_p, areal damage fraction f_d, and size distributions) [9]. For aluminium alloys in chloride media, pit development often proceeds through metastable pits that may repassivate and stable pits that propagate; reinforcement-induced heterogeneity can shift this balance by increasing the likelihood that a pit becomes stable [23].

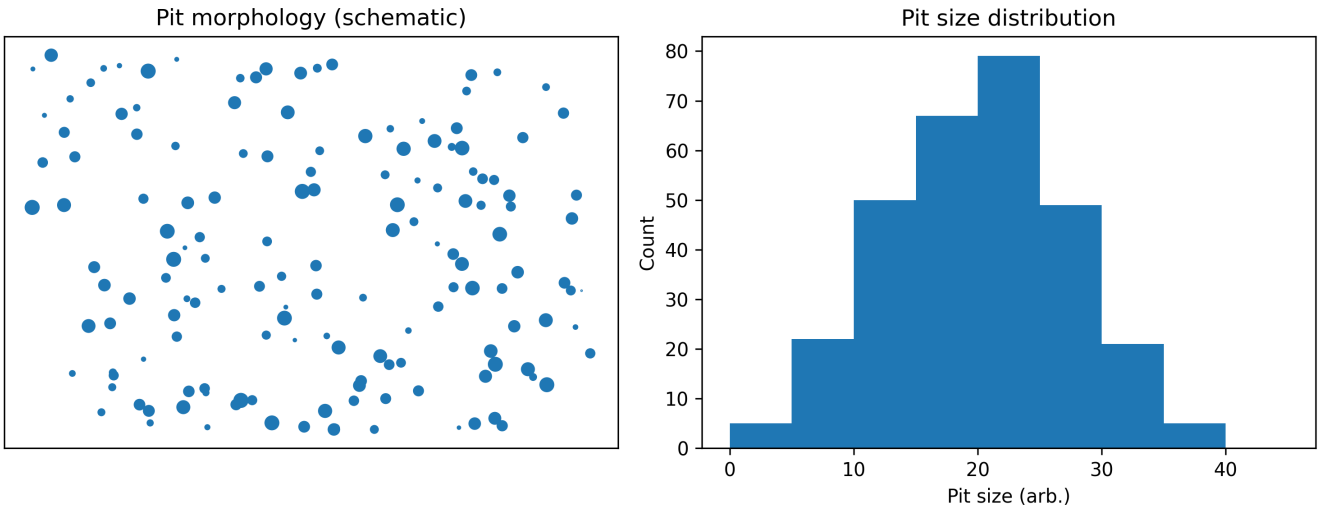

Figure 6: Representative pit morphology and statistics

For the GO composite, reinforcement clusters and interfacial discontinuities can provide preferential pit initiation sites because they offer locally higher chloride concentration, lower oxygen diffusion, and higher film strain or defect density [17, 22]. Pits near clusters may also coalesce more readily, creating larger damaged regions than would be expected from a uniform pit field [9]. In Al_2O_3@GO, the expected microstructural benefit is a reduced tendency for pit initiation at reinforcement-rich regions and a more uniform distribution of smaller pits, reflected by reduced N_p and/or reduced tail of the pit-size distribution.

A critical point is that f_d alone may not capture worst-case integrity loss; therefore, reporting the maximum pit diameter or a high percentile metric (e.g., D_{90}) is recommended because hardness loss and local weakening may be dominated by a small number of large pits [22]. The combined reporting of N_p, f_d, and pit-size distribution enables robust linkage to electrochemical indicators [20]. For example, conditions with low-frequency impedance reductions and low n values often coincide with more heterogeneous and roughened surfaces consistent with higher pit density and more severe localized attack [20, 21].

3.6 Hardness degradation and hardness-retention mapping

Hardness measurements translate corrosion damage into a mechanically meaningful metric. Figure 7 should be interpreted by considering both the mean hardness shift and the spatial variability after exposure. In pit-dominated corrosion, hardness reduction can arise from (i) removal of load-bearing material at the surface, (ii) formation of microcracks linked to pits which reduce constraint under indentation, and (iii) heterogeneous surface roughness and undercutting that reduce effective contact support. As a result, hardness measurements typically become more scattered after exposure, and this scatter is itself informative because it reflects heterogeneity in damage severity [23].

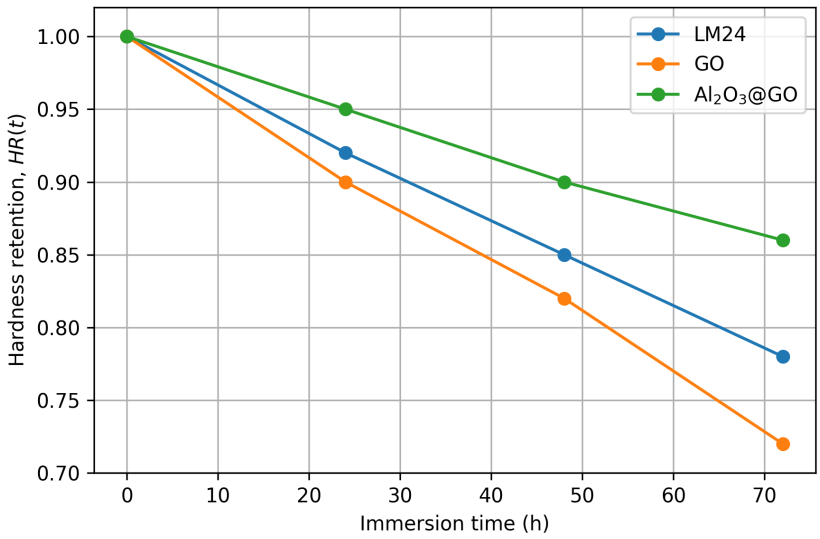

Figure 7: Hardness mapping and retention vs. immersion time

For the baseline (unexposed) materials, GO addition may increase hardness through dispersion strengthening and microstructural refinement when dispersion is adequate [15]. After immersion, hardness retention reflects the competition between any strengthening benefit and corrosion-induced surface weakening [22]. The Al_2O_3@GO approach is expected to improve hardness retention primarily by reducing localized damage severity (smaller pits, less coalescence), thus limiting the emergence of weak surface regions that dominate indentation response.

To formalize the damage–property linkage, hardness retention is defined as

$$HR(t) = \frac{HV(t)}{HV(0)}, \tag{5}$$

and correlated with areal damage fraction through a first-order model

$$HR(t) \approx 1 - \alpha\, f_d(t), \tag{6}$$

where α is obtained by regression. Here α is interpretable as an effective "damage sensitivity" of hardness: higher α implies that a given pit-damage fraction translates into greater hardness loss, consistent with deeper undercutting, pit-induced cracking, or more severe local weakening [22]. Importantly, comparing α across GO and Al_2O_3@GO provides a compact screening metric: even if two systems show similar f_d, the one with lower α has less mechanically harmful damage

morphology [22]. Reporting confidence bounds on α (from regression) is recommended because pitting metrics can be noisy [22].

3.7 Mechanistic interpretation

Taken together, the results support a unified pathway linking processing, interfacial state, electrochemical response, localized damage, and mechanical degradation [17, 20]. Reinforcement-related heterogeneities—including clusters, interfacial voids, and chemically distinct zones—act as weak points in the passive film and favor chloride-assisted breakdown [10,22]. Once a pit forms, local hydrolysis acidifies the pit environment and chloride migrates inward to maintain charge balance, sustaining dissolution and enabling pit growth [9,10]. Pit growth, coalescence, and underfilm attack reduce the effective load-bearing area and introduce microcracking, leading to lower and more scattered hardness measurements [22,23].

Within this framework, the functional role of Al_2O_3@GO is to interrupt the most detrimental interfacial pathways while preserving the dispersion-related mechanical benefits of GO. The alumina interlayer is chemically stable in the tested environment relative to direct Al–C contact sites and is compatible with the native oxide film, reducing interfacial electrochemical discontinuities [13,17]. Consequently, successful mitigation should manifest consistently across measurement modes: lower i_{corr} (kinetic suppression), higher R_p and more ideal capacitive behaviour (improved film stability and reduced heterogeneity), reduced N_p and diminished large-pit tail (suppressed localized breakdown and growth), and higher hardness retention with reduced post-exposure scatter (mechanically less harmful damage) [20–22]. If the microstructural/chemical characterization confirms reduced evidence of interfacial reaction products and the electrochemical indicators show improved passivation, the combined dataset provides direct validation that interfacial engineering is an effective route to improving chloride durability in Al/GO cast nanocomposites [13,17].

4. Conclusion

This study demonstrates that interfacial engineering of graphene oxide with a thin alumina layer offers an effective pathway to improve the corrosion durability and surface mechanical stability of LM24 aluminium nanocomposites produced by ultrasonic gravitational stir casting. By integrating immersion mass-loss testing with electrochemical characterization, the work shows that corrosion performance cannot be fully assessed by weight loss alone and must be interpreted in terms of corrosion kinetics and passive-film stability. Quantification of pit morphology and statistics establishes localized pitting as the dominant degradation mode and provides a direct link between electrochemical response and mechanical weakening. The introduction of Al_2O_3@GO is shown to mitigate reinforcement-associated heterogeneities, reduce pit initiation and growth severity, and enhance polarization resistance, leading to improved hardness retention after chloride exposure. Overall, the results highlight interfacial modification as a critical design variable for translating the mechanical advantages of graphene-based reinforcements into reliable performance in chloride-rich service environments.

References

[1] Clyne, T. W., & Withers, P. J. (1993). *An Introduction to Metal Matrix Composites*. Cambridge university press.
[2] Surappa, M. K. (2003). Aluminium matrix composites: Challenges and opportunities. *Sadhana, 28*(1), 319-334.
[3] Narayanan, S., Sozhamannan, G. G., Hemalatha, K., Velmurugan, K., & Venkatachalapathy, V. S. K. (2021). Corrosion and hardness behaviour of Al/GO nanocomposites processed by the ultrasonic gravitational stir casting method. *International Journal of Corrosion, 2021*(1), 6658186.
[4] Hashim, J., Looney, L., & Hashmi, M. S. J. (1999). Metal matrix composites: production by the stir casting method. *Journal of Materials Processing Technology, 92*, 1-7.
[5] Smith, A. T., LaChance, A. M., Zeng, S., Liu, B., & Sun, L. (2019). Synthesis, properties, and applications of graphene oxide/reduced graphene oxide and their nanocomposites. *Nano Materials Science, 1*(1), 31-47.
[6] Geim, A. K., & Novoselov, K. S. (2007). The rise of graphene. *Nature Materials, 6*(3), 183-191.
[7] Eskin, G. I. (1995). Cavitation mechanism of ultrasonic melt degassing. *Ultrasonics Sonochemistry, 2*(2), S137-S141.
[8] Eskin, G. I. (1998). *Ultrasonic Treatment of Light Alloy Melts*. CRC press.
[9] Szklarska-Smialowska, Z. (1999). Pitting corrosion of aluminum. *Corrosion Science, 41*(9), 1743-1767.
[10] Frankel, G. S. (1998). Pitting corrosion of metals: a review of the critical factors. *Journal of the Electrochemical Society, 145*(6), 2186.
[11] Pardo, A., Merino, M. C., Coy, A. E., Arrabal, R., Viejo, F., & Matykina, E. (2008). Corrosion behaviour of magnesium/aluminium alloys in 3.5 wt.% NaCl. *Corrosion Science, 50*(3), 823-834.
[12] Mansfeld, F. (1990). Electrochemical impedance spectroscopy (EIS) as a new tool for investigating methods of corrosion protection. *Electrochimica Acta, 35*(10), 1533-1544.
[13] Macdonald, D. D. (1992). The point defect model for the passive state. *Journal of the Electrochemical Society, 139*(12), 3434.
[14] Aghajanian, M. K., Rocazella, M. A., Burke, J. T., & Keck, S. D. (1991). The fabrication of metal matrix composites by a pressureless infiltration technique. *Journal of Materials Science, 26*(2), 447-454.
[15] Tjong, S. C. (2007). Novel nanoparticle-reinforced metal matrix composites with enhanced mechanical properties. *Advanced Engineering Materials, 9*(8), 639-652.
[16] Stankovich, S., Dikin, D. A., Dommett, G. H., Kohlhaas, K. M., Zimney, E. J., Stach, E. A., ... & Ruoff, R. S. (2006). Graphene-based composite materials. *Nature, 442*(7100), 282-286.
[17] Landolt, D. (2007). *Corrosion and Surface Chemistry of Metals*. EPFL press.
[18] Kudla, F., & Marya, M. (2024, March). An Environmental Performance Comparison of Premium vs. Standard Grades Used in Non-Magnetic Drill Collars. In *Conference* 2024 (pp. 1-15). Association for Materials Protection and Performance.

[19] ASTM, G. (2014). *Standard Reference Test Method for Making Potentiodynamic Anodic Polarization Measurements*. West Conshohocken (PA): ASTM International.
[20] Orazem, M. E., & Tribollet, B. (2008). Electrochemical impedance spectroscopy. *New Jersey, 1*(906), 383-389.
[21] Jorcin, J. B., Orazem, M. E., Pébère, N., & Tribollet, B. (2006). CPE analysis by local electrochemical impedance spectroscopy. *Electrochimica Acta, 51*(8-9), 1473-1479.
[22] Cramer, S. D., & Covino Jr, B. S. (Eds.). (2003). *Corrosion: Fundamentals, Testing, and Protection*. ASM international.
[23] Hardness, A. B. (1999). *Standard Test Method for Microindentation Hardness of Materials*. ASTM Committee: West Conshohocken, PA, USA, 384, 399.